

---

# Defending Variational Autoencoders from Adversarial Attacks with MCMC

---

**Anna Kuzina**

Vrije Universiteit Amsterdam  
a.kuzina@vu.nl

**Max Welling**

Universiteit van Amsterdam  
m.welling@uva.nl

**Jakub M. Tomczak**

Vrije Universiteit Amsterdam  
j.m.tomczak@vu.nl

## Abstract

Variational autoencoders (VAEs) are deep generative models used in various domains. VAEs can generate complex objects and provide meaningful latent representations, which can be further used in downstream tasks such as classification. As previous work has shown, one can easily fool VAEs to produce unexpected latent representations and reconstructions for a visually slightly modified input. Here, we examine several objective functions for adversarial attacks construction, suggest metrics assess the model robustness, and propose a solution to alleviate the effect of an attack. Our method utilizes the Markov Chain Monte Carlo (MCMC) technique in the inference step and is motivated by our theoretical analysis. Thus, we do not incorporate any additional costs during training or we do not decrease the performance on non-attacked inputs. We validate our approach on a variety of datasets (MNIST, Fashion MNIST, Color MNIST, CelebA) and VAE configurations ( $\beta$ -VAE, NVAE, TC-VAE) and show that it consistently improves the model robustness to adversarial attacks.

## 1 Introduction

Variational Autoencoders (VAEs) (Kingma & Welling, 2014; Rezende et al., 2014) are deep generative models used in various domains. Recently, it was shown that Variational Autoencoders with hierarchical structure (Ranganath et al., 2016), coupled with skip-connections (Maaløe et al., 2019; Sønderby et al., 2016), can generate high-quality images (Vahdat & Kautz, 2020; Child, 2021). An interesting trait of VAEs is that they allow learning meaningful latent space induced by the encoder. These latent representations are commonly used in downstream tasks (Bengio et al., 2013; Higgins et al., 2017). These motivates us to explore the *robustness* of the resulting latent representations to understand the capabilities and potential vulnerabilities of VAEs better. *Adversarial attacks* constitute one way to assess the robustness of a deep neural network. Robustness to the attacks is a crucial property for VAEs, especially in such applications as anomaly detection (An & Cho, 2015; Maaløe et al., 2019) or data compression (Ballé et al., 2018; Habibian et al., 2019). Here, we focus on adversarial attacks in the VAE framework.

The main questions about adversarial attacks for VAEs are how they could be formulated and how they could be prevented. Gondim-Ribeiro et al. (2018) propose to minimize the KL-divergence between an adversarial input and a target input to learn an adversarial attack for the standard VAE model. Kuzina et al. (2021) show that similar strategy can be used to attack hierarchical VAEs. To counteract the adversarial attacks, Willetts et al. (2021) suggest using a modified VAE objective,  $\beta$ -TCVAE, that increases VAE robustness, especially when coupled with the hierarchical structure. Further, Camuto et al. (2021) show that  $\beta$ -VAEs tend to be more robust to adversarial attacks in terms of the  $r$ -metric proposed therein. Barrett et al. (2021) show that the adversarial robustness can be achieved by constraining the Lipschitz constant of the encoder and the decoder. Cemgil et al. (2019, 2020) introduce modifications in the VAE framework that allow for better robustness against the adversarial attacks on downstream classification tasks. In our work, we test both  $\beta$ -VAE,  $\beta$ -TCVAE

and a hierarchical VAE and propose a defence strategy that significantly improves robustness against attacks on the encoder and the downstream classification task.

The adversarial attack on VAE is usually formulated as an additive perturbation  $\varepsilon$  of the real data point  $\mathbf{x}^r$  so that the resulting point is perceived by the model as if it is a totally different image (either during reconstruction or in the downstream classification task). In Figure 1, we depict an example of the attack on the encoder: the reference point  $\mathbf{x}^r$  and the adversarial point  $\mathbf{x}^a$  are almost indistinguishable, but they are encoded into different places in the latent space. As a result, their reconstructions also differ significantly.

In this paper, we formulate the following hypothesis: *An adversarial attack maps the input to a latent region with a lower probability mass assigned by the true posterior (proportional to the conditional likelihood times the marginal over latents) and, as a result, we obtain incorrect reconstructions.* Therefore, a potential defence strategy may rely on running a Markov chain to move the latent representation back to a more probable latent region. Such a defence is reasonable because we do not modify the training procedure or the model itself, we only insert a correction procedure. As a result, we propose to counteract adversarial attacks by enhancing the variational inference with Markov Chain Monte Carlo (MCMC) sampling. The toy experiment depicted in the Figure 1 shows that the latent code of the adversarial input (red star) after applying MCMC (purple circle) moves closer to the latent code of the reference point (orange star).

The contribution of this work is the following:

- We propose to use an MCMC technique during inference to correct the adversarial attack.
- We show theoretically that the application of an MCMC technique could indeed help to counteract adversarial attacks (Theorem 3).
- We indicate empirically that the previously proposed strategies to counteract adversarial attacks do not generalize well across various datasets.
- We show empirically that the proposed approach (i.e. a VAE with an MCMC chain during inference) outperforms all baselines by a significant margin.

## 2 Background

## 2.1 Variational Autoencoders

Let us consider a vector of observable random variables,  $\mathbf{x} \in \mathcal{X}^D$  (e.g.,  $\mathcal{X} = \mathbb{R}$ ) sampled from the empirical distribution  $p_e(\mathbf{x})$ , and vectors of latent variables  $\mathbf{z}_k \in \mathbb{R}^{M_k}$ ,  $k = 1, 2, \dots, K$ . First, we focus on a model with  $K = 1$  and the joint distribution  $p_\theta(\mathbf{x}, \mathbf{z}) = p_\theta(\mathbf{x}|\mathbf{z})p(\mathbf{z})$ . The marginal likelihood is then equal to  $p_\theta(\mathbf{x}) = \int p_\theta(\mathbf{x}, \mathbf{z})d\mathbf{z}$ . VAEs exploit variational inference (Jordan et al., 1999) with a family of variational posteriors  $\{q_\phi(\mathbf{z}|\mathbf{x})\}$ , also referred to

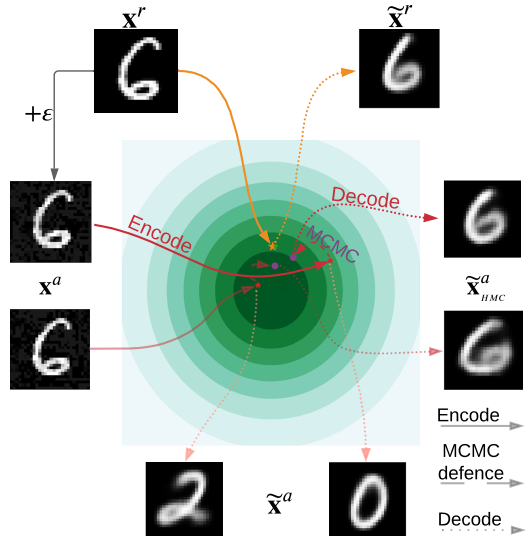


Figure 1: Example of an unsupervised encoder attack on VAE with 2D latent space and the proposed defence. Given a single reference point  $\mathbf{x}^r$  we learn additive perturbation  $\varepsilon$ , s.t. perturbed input  $\mathbf{x}^a$  has the most different latent code and, therefore, the reconstruction  $\tilde{\mathbf{x}}^a$ . We observe that a single reference point can be mapped to extremely different regions of the latent space but using MCMC we are able to move them closer to the initial position so that the reconstruction  $\tilde{\mathbf{x}}_{HMC}^a$  is similar to the initial one  $\tilde{\mathbf{x}}^r$ .

Table 1: Different types of attacks on the VAE. We denote  $g_\theta(z)$  the deterministic mapping induced by decoder  $p_\theta(x|z)$  and as  $p_\psi(y|z)$  classification model in the latent space (downstream task).

\* Only used during VAE training

	REFERENCE	$f(x)$	$\Delta [A, B]$	$\ \cdot\ _p$	TYPE
Latent Space Attack	Gondim-Ribeiro et al. (2018); Willetts et al. (2021); Barrett et al. (2021)	$q_\phi(\cdot x)$	$\text{KL}[A\ B]$	2	Supervised
Unsupervised Encoder Attack	Kuzina et al. (2021)	$q_\phi(\cdot x)$	$\text{SKL}[A\ B]$	2	Unsupervised
Targeted Output Attack	Gondim-Ribeiro et al. (2018)	$g_\theta(\tilde{z}), \tilde{z} \sim q_\phi(\cdot x)$	$\ A - B\ _2$	2	Supervised
Maximum Damage Attack	(Barrett et al., 2021; Camuto et al., 2021)	$g_\theta(\tilde{z}), \tilde{z} \sim q_\phi(\cdot x)$	$\ A - B\ _2$	2	Unsupervised
Projected Gradient Descent Attack <sup>*</sup>	(Cemgil et al., 2019)	$q_\phi(\cdot x)$	$\mathcal{WD}[A, B]$	inf	Unsupervised
Adversarial Accuracy	(Cemgil et al., 2019, 2020)	$p_\psi(y \tilde{z}), \tilde{z} \sim q_\phi(\cdot x)$	CROSS ENTROPY	inf	Unsupervised

as encoders, that results in a tractable objective function, i.e., Evidence Lower BOund (ELBO):  $\mathcal{L}(\phi, \theta) = \mathbb{E}_{p_\theta(\mathbf{x})} (\mathbb{E}_{q_\phi(\mathbf{z}|\mathbf{x})} \ln p_\theta(\mathbf{x}|\mathbf{z}) - \text{KL}[q_\phi(\mathbf{z}|\mathbf{x})\|p(\mathbf{z})])$ .

$\beta$ -VAE (Higgins et al., 2016) uses a slightly modifier objective, weighting the second term by  $\beta > 0$ . In the case of  $K > 1$ , we consider a hierarchical latent structure with the generative model of the following form:  $p_\theta(\mathbf{x}, \mathbf{z}_1, \dots, \mathbf{z}_K) = p_\theta(\mathbf{x}|\mathbf{z}_1, \dots, \mathbf{z}_K) \prod_{k=1}^K p_\theta(\mathbf{z}_k|\mathbf{z}_{>k})$ . There are various possible formulations of the family of variational posteriors, however, here we follow the proposition of Sønderby et al. (2016) with autoregressive inference model, namely:

$$q_\phi(\mathbf{z}_1, \dots, \mathbf{z}_K|\mathbf{x}) = q_\phi(\mathbf{z}_K|\mathbf{x}) \prod_{k=1}^{K-1} q_{\theta, \phi}(\mathbf{z}_k|\mathbf{z}_{>k}, \mathbf{x}). \quad (1)$$

This formulation was used in NVAE (Vahdat & Kautz, 2020). Because of the top-down structure, it allows sharing data-dependent information between the inference model and the generative model.

## 2.2 Adversarial attacks

An *adversarial attack* is a slightly deformed data point that results in an undesired or unpredictable performance of a model (Goodfellow et al., 2014). In this work, we focus on the attacks that are constructed as an additive perturbation of the real data point  $\mathbf{x}^r$  (which we will refer to as *reference*):

$$\mathbf{x}^a = \mathbf{x}^r + \varepsilon, \text{ where} \quad (2)$$

$$\|\varepsilon\|_p \leq \delta. \quad (3)$$

$\delta$  is a radius of the attack. The additive perturbation  $\varepsilon$  is chosen so that the attacked point does not differ from the reference point too much. It is a solution to an optimization problem solved by the attacker. The optimization problem could be formulated in various manners by optimizing different objectives and by having specific constraints and/or assumptions.

**Attack construction** Let  $f(x)$  be part of the model available to the attacker. In the case of VAE, this, for example, may be an encoder network or encoder with the downstream classifier in the latent space. The attacker uses a distance metric  $\Delta$  to learn an additive perturbation to a reference point. We consider two settings: *unsupervised* and *supervised*. In the former case, the perturbation is supposed to incur the largest possible change in  $f$ :

$$\varepsilon = \arg \max_{\|\varepsilon\|_p \leq \delta} \Delta [f(\mathbf{x}^r + \varepsilon), f(\mathbf{x}^r)]. \quad (4)$$

The latter setting requires a *target point*  $\mathbf{x}^t$ . The perturbation attempts to match output for the target and the attacked points, namely:

$$\varepsilon = \arg \min_{\|\varepsilon\|_p \leq \delta} \Delta [f(\mathbf{x}^r + \varepsilon), f(\mathbf{x}^t)]. \quad (5)$$

There are different ways to select  $f$  and  $\Delta$  in the literature. Furthermore, different  $L_p$ -norms can be used to restrict the radius of the attack. Table 1 summarizes recent works on adversarial attacks on VAE.

In this work, we focus on attacking the encoder and the downstream classification task using unsupervised adversarial attacks. In the former, we maximize the symmetric KL-divergence to get the point with the most unexpected latent code and, therefore, the reconstruction. In the latter, the latent code is passed to a classifier. The attack is trained to change the class of the point by maximizing the cross-entropy loss. However, the defence strategy that we propose in the next section is not limited to these setups since it is agnostic to how the attack was trained.

**Robustness measures** To measure the robustness of the VAE as well as the success of the proposed defence strategy, we focus on two metrics: MSSSIM and Adversarial accuracy.

For latent space attacks we follow (Kuzina et al., 2021) in using Multi-Scale Structural Similarity Index Measure (MSSSIM) (Wang et al., 2003). We calculate  $\text{MSSSIM}[\tilde{\mathbf{x}}^r, \tilde{\mathbf{x}}^a]$ , i.e., the similarity between reconstructions of  $\mathbf{x}^r$  and the corresponding  $\mathbf{x}^a$ . We do not report the similarity between a reference and the corresponding adversarial input, since this value is the same for all the considered models (for a given attack radius). A successful adversarial attack would have small  $\text{MSSSIM}[\tilde{\mathbf{x}}^r, \tilde{\mathbf{x}}^a]$ .

For the attacks on the downstream classifier, we follow (Cemgil et al., 2019, 2020) and calculate adversarial accuracy. For a given trained VAE model, we firstly train a linear classifier using latent codes as a feature. Afterwards, the attack is trained to fool the classifier. Adversarial accuracy is a proportion of points for which the attack was unsuccessful. Namely, when the predicted class of the reference and corresponding adversarial point are the same.

### 3 Preventing adversarial attacks with MCMC

**Assumptions and the hypothesis** We consider a scenario in which an attacker has access to the VAE encoder and, where relevant, to the downstream classification model. Above, we presented in detail how an attack could be performed. We assume that modifying these components is forbidden, but it is possible to add elements that the attacker has no access to.

We hypothesize that *the adversarial attacks result in incorrect reconstructions because the latent representation of the adversarial input lands in a region with a lower probability mass assigned by the true posterior*. A potential solution to this issue would be to bring the latents "back" to a highly probable region. Since the adversarial attack destroys the input irreversibly, at first sight it seems impossible to reconstruct the latent representation of the reference point.

**The proposed solution** In order to steer the latents towards high probability regions, we propose to utilize an MCMC method during inference time. Since we are not allowed to modify the VAE or its learning procedure, this is a reasonable procedure from the defender's perspective. Another positive outcome of such an approach is that in a case of no attack, the latents given by the MCMC sampling will be closer to the mean of the posterior, thus, the reconstruction should be sharper or, at least, not worse. (Note that the variational posterior approximates the true posterior from which the MCMC procedure samples.)

Now, the naturally arising question is whether applying the MCMC could indeed help us in the case of an adversarial attack. To further analyze the proposed approach, we start with showing the following lemma:

**Lemma 1** *Consider true posterior distributions of the latent code  $\mathbf{z}$  for a data point  $\mathbf{x}^r$  and its corrupted version  $\mathbf{x}^a$ . Then the KL-divergence between these two posteriors could be expressed using the small  $o$  notation in terms of the radius of the attack, namely:*

$$\text{KL}[p_\theta(\mathbf{z}|\mathbf{x}^r) \| p_\theta(\mathbf{z}|\mathbf{x}^a)] = o(\|\varepsilon\|). \quad (6)$$

*Proof* See Appendix A.

According to Lemma 1, the difference (in the sense of the Kullback-Leibler divergence) between the true posteriors for a data point  $\mathbf{x}$  and its corrupted version  $\tilde{\mathbf{x}}$  is proportional to the norm of the noise (attack). This result is rather intuitive because the stronger is the noise, the larger is the difference between the latent representations.

Next, the crucial step to show is whether we can quantify somehow the difference between the distribution over latents for  $\mathbf{x}^a$  after applying the MCMC,  $q^{(t)}(\mathbf{z}|\mathbf{x}^a)$ , and the variational distribution

for  $\mathbf{x}^r$ ,  $q_\phi(\mathbf{z}|\mathbf{x}^r)$ . We provide an important upper-bound for the Total Variation distance (TV)<sup>1</sup> between  $q^{(t)}(\mathbf{z}|\mathbf{x}^a)$  and  $q_\phi(\mathbf{z}|\mathbf{x}^r)$  in the following lemma:

**Lemma 2** *The Total Variation distance (TV) between the variational posterior with MCMC for a given corrupted point  $\mathbf{x}^a$ ,  $q^{(t)}(\mathbf{z}|\mathbf{x}^a)$ , and the variational posterior for a given data point  $\mathbf{x}^r$ ,  $q_\phi(\mathbf{z}|\mathbf{x}^r)$ , can be upper bounded by the sum of the following three components:*

$$\begin{aligned} \text{TV} \left[ q^{(t)}(\mathbf{z}|\mathbf{x}^a), q_\phi(\mathbf{z}|\mathbf{x}^r) \right] &\leq \text{TV} \left[ q^{(t)}(\mathbf{z}|\mathbf{x}^a), p_\theta(\mathbf{z}|\mathbf{x}^a) \right] \\ &\quad + \sqrt{\frac{1}{2} \text{KL} [p_\theta(\mathbf{z}|\mathbf{x}^r) \| p_\theta(\mathbf{z}|\mathbf{x}^a)]} \\ &\quad + \sqrt{\frac{1}{2} \text{KL} [q_\phi(\mathbf{z}|\mathbf{x}^r) \| p_\theta(\mathbf{z}|\mathbf{x}^r)]}. \end{aligned} \quad (7)$$

*Proof* See Appendix A.

The difference expressed by  $\text{TV} [q^{(t)}(\mathbf{z}|\mathbf{x}^a), q_\phi(\mathbf{z}|\mathbf{x}^r)]$  is thus upper-bounded by the following three components:

- The TV between  $q^{(t)}(\mathbf{z}|\mathbf{x}^a)$  and the real posterior for the corrupted image,  $p_\theta(\mathbf{z}|\mathbf{x}^a)$ . Theoretically, if  $t \rightarrow \infty$ ,  $q^{(\infty)}(\mathbf{z}|\mathbf{x}^a) = p_\theta(\mathbf{z}|\mathbf{x}^a)$  and, hence,  $\text{TV} [q^{(\infty)}(\mathbf{z}|\mathbf{x}^a), p_\theta(\mathbf{z}|\mathbf{x}^a)] = 0$ .
- The second component is the square root of the KL-divergence between the real posteriors for the image and its corrupted counterpart. Lemma 1 gives us some information about this quantity.
- The last element, the square root of  $\text{KL} [q_\phi(\mathbf{z}|\mathbf{x}^r) \| p_\theta(\mathbf{z}|\mathbf{x}^r)]$ , quantifies the *approximation gap* Cremer et al. (2018), i.e., the difference between the best variational posterior and the true posterior. This quantity has no direct connection with adversarial attacks. However, as we can see, using a rich family of variational posteriors can help us obtain a tighter upper-bound. In other words, taking flexible variational posteriors allows to counteract attacks. This finding is in line with the papers that propose to use hierarchical VAEs as the means for preventing adversarial attacks Willetts et al. (2021).

Eventually, by applying Lemma 1 to Lemma 2, we obtain the following result:

**Theorem 3** *The upper bound on the total variation distance between samples from MCMC for a given corrupted point  $\mathbf{x}^a$ ,  $q^{(t)}(\mathbf{z}|\mathbf{x}^a)$ , and the variational posterior for the given real point  $\mathbf{x}^r$ ,  $q_\phi(\mathbf{z}|\mathbf{x}^r)$ , is the following:*

$$\begin{aligned} \text{TV} \left[ q^{(t)}(\mathbf{z}|\mathbf{x}^a), q_\phi(\mathbf{z}|\mathbf{x}^r) \right] &\leq \text{TV} \left[ q^{(t)}(\mathbf{z}|\mathbf{x}^a), p_\theta(\mathbf{z}|\mathbf{x}^a) \right] \\ &\quad + \sqrt{\frac{1}{2} \text{KL} [q_\phi(\mathbf{z}|\mathbf{x}^r) \| p_\theta(\mathbf{z}|\mathbf{x}^r)]} \\ &\quad + o(\sqrt{\|\varepsilon\|}). \end{aligned} \quad (8)$$

*Proof* See Appendix A.

As discussed already, the first component gets smaller with more steps of the MCMC. The second component could be treated as a *bias* of the family of variational posteriors. Finally, there is the last element that corresponds to a constant error that is unavoidable. However, this term decays faster than the square root of the attack radius.

**Specific implementation of the proposed approach** In our approach, we propose to use the Hamiltonian Monte Carlo (HMC) (Betancourt, 2017; Duane et al., 1987). Once the VAE is trained, the attacker calculates an adversarial point  $\mathbf{x}^a$  using the encoder of the VAE. After the attack, the latent representation of  $\mathbf{x}^a$  is calculated,  $\mathbf{z}^a$ , and used as the initialization of HMC.

<sup>1</sup>The Total Variation fulfills the triangle inequality and it is a proper distance measure.

In HMC, the target (unnormalized) distribution is  $p(\mathbf{x}^a|\mathbf{z})p(\mathbf{z})$ . The Hamiltonian is then the energy of the joint distribution of  $\mathbf{z}$  and the auxiliary variable  $\mathbf{p}$ , that is:

$$H(\mathbf{z}, \mathbf{p}) = U(\mathbf{z}) + K(\mathbf{p}), \quad (9)$$

$$U(\mathbf{z}) = -\ln p_\theta(\mathbf{x}^a|\mathbf{z}) - \ln p(\mathbf{z}), \quad (10)$$

$$K(\mathbf{p}) = -\frac{1}{2}\mathbf{p}^T\mathbf{p}. \quad (11)$$

When applying the proposed defence to hierarchical models, we update all the latent variables simultaneously. That is, we have  $\mathbf{z} = \{\mathbf{z}_1, \dots, \mathbf{z}_K\}$  and

$$U(\mathbf{z}) = -\ln p_\theta(\mathbf{x}^a|\mathbf{z}) - \sum_{k=1}^K \ln p_\theta(\mathbf{z}_k|\mathbf{z}_{k+1}). \quad (12)$$

Eventually, the resulting latents from the HMC are decoded.

The steps of the whole process are presented below:

1. (*Defender*) Train a VAE:  $q_\phi(\mathbf{z}|\mathbf{x})$ ,  $p(\mathbf{z})$ ,  $p_\theta(\mathbf{x}|\mathbf{z})$ .
2. (*Attacker*) For given  $\mathbf{x}^r$ , calculate the attack  $\mathbf{x}^a$  using the criterion equation 4 or equation 5.
3. (*Defender*) Initialize the latent code  $\mathbf{z} := \mathbf{z}_0$ , where  $\mathbf{z}_0 \sim q_\phi(\mathbf{z}|\mathbf{x}^a)$ . Then, run  $T$  steps of HMC (Algorithm 1) with the step size  $\eta$  and  $L$  leapfrog steps.

The resulting latent code  $\mathbf{z}$  can be passed to the decoder or to the downstream classification task.

## 4 Experiments

In this section, we experimentally evaluate performance of the proposed approach. We perform experiments on a variety of VAE models ( $\beta$ -VAE,  $\beta$ -TCVAE and NVAE) and datasets (MNIST, Fashion MNIST, Color MNIST, CelebA).

### 4.1 VAE, $\beta$ -VAE and $\beta$ -TCVAE

First, we consider attacks on VAE with a single level of latent variables.

**Datasets** VAE is trained on the MNIST, Fashion MNIST (Xiao et al., 2017) and Color MNIST datasets. Following (Cemgil et al., 2019), we construct the Color MNIST dataset from MNIST by artificially coloring each image with seven colors (all corners of RGB cube except for black).

**Models** We train conventional fully convolutional VAE, as well as  $\beta$ -VAE (Higgins et al., 2016) and  $\beta$ -TCVAE (Kim & Mnih, 2018; Chen et al., 2018). Both  $\beta$ -VAE and  $\beta$ -TCVAE modify the ELBO objective to encourage disentanglement.  $\beta$ -VAE weighs the KL-term in the ELBO with  $\beta > 0$ . It is said that the larger values of  $\beta$  encourage disentangling of latent representations (Chen et al., 2018) and improve the model robustness as observed by Camuto et al. (2021).  $\beta$ -TCVAE puts a higher weight on the total correlation (TC) term of the ELBO. Penalization of the total correlation was shown to increase the robustness of VAE adversarial attacks (Willetts et al., 2021).

In Appx. C.1 we provide details of the architecture, optimization, and results on the test dataset for VAE trained with different values of  $\beta$ . We note that the optimal value in terms of the negative

Table 2: Robustness results on MNIST and Fashion MNIST datasets. We perform unsupervised attack with radius 0.1 (top) and 0.2 (bottom). We attack the encoder (left) and the downstream classification task (right). Higher values correspond to more robust models.

<sup>†</sup> Our implementation.

			MSSSIM[ $\tilde{\mathbf{x}}^r, \tilde{\mathbf{x}}^a$ ] ↑		ADVERSARIAL ACCURACY ↑			MSE
			0.1	0.2	0.0	0.1	0.2	
MNIST	VAE		0.70 (0.02)	0.36 (0.03)	<b>0.90</b> (0.04)	0.08 (0.04)	0.05 (0.03)	<b>578.66</b>
	VAE + HMC		<b>0.88</b> (0.01)	<b>0.76</b> (0.02)	<b>0.90</b> (0.04)	<b>0.25</b> (0.03)	<b>0.19</b> (0.03)	<b>578.66</b>
	$\beta$ -TCVAE <sup>†</sup>		0.70 (0.02)	0.46 (0.03)	0.86 (0.05)	0.05 (0.03)	0.03 (0.02)	828.39
FASHION MNIST	VAE		0.59 (0.03)	0.47 (0.03)	0.78 (0.06)	0.00 (0.01)	0.01 (0.01)	<b>814.2</b>
	VAE + HMC		<b>0.66</b> (0.03)	<b>0.54</b> (0.03)	0.78 (0.06)	<b>0.14</b> (0.02)	<b>0.13</b> (0.02)	<b>814.2</b>
	$\beta$ -TCVAE <sup>†</sup>		0.52 (0.03)	0.42 (0.03)	<b>0.84</b> (0.05)	0.00 (0.01)	0.02 (0.02)	980.4

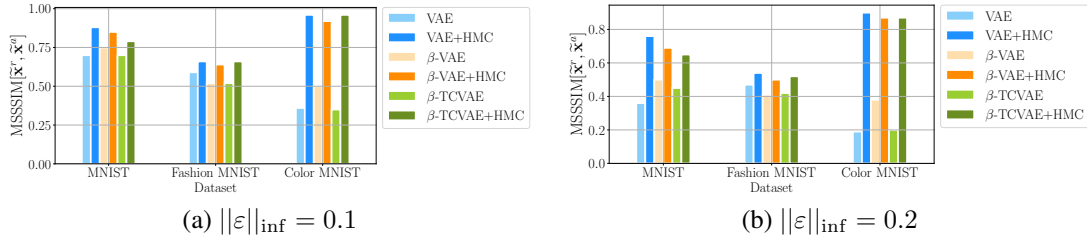


Figure 2: Improvement of the Reconstruction Similarity after the proposed defence. We fix the attack radius to be equal to (a) 0.1 and (b) 0.2.

log-likelihood (NLL) is always  $\beta = 1$ . Larger values of  $\beta$  are supposed to improve robustness in exchange for the reconstruction quality.

When evaluating the robustness of  $\beta$ -VAE and  $\beta$ -TCVAE, we train models with  $\beta \in \{2, 5, 10\}$ . Then we select the value of  $\beta$ , which provides the most robust model in terms of the used metric. Then we apply our defence strategy to this model to observe the potential performance improvement.

**Attacks on the Encoder** In the first setup, we assume that the attacker has access to the encoder of the model  $q_\phi(z|x)$ . We have used the projected gradient descent (PGD) with 50 steps to maximize the symmetric KL-divergence in the unsupervised setting (equation 4). We train ten adversarial attacks (with different random initialization) for each reference point. See Appendix C.2 for the list of all the hyperparameters used during the attack and defence.

In Figure 2, we show how similarity between the reconstructions of the reference and adversarial points increases after the proposed defence is applied. This metric consistently improves for all the datasets, radii and models considered. In Figure 5, we plot two examples for each of the datasets considered (see subsection 4.2 for more details on CelebA experiments). The first two columns contain reference points and their reconstructions (columns a & b). Then we plot the adversarial input (column c) and its reconstruction without the defence (column d). Finally, we provide the reconstruction with the defence applied (column e) that is much closer to the reconstruction of the reference point.

**Attacks on the downstream task** In the next setup, we examine how the proposed approach can defend against the attacks on the downstream tasks in the latent space. For this purpose, we follow the procedure from (Cemgil et al., 2019, 2020). After the VAE is trained, we learn a linear classifier using the mean mappings as features. For MNIST and Fashion MNIST datasets, we have a 10-class classification problem (digits in the former and pieces of clothing in the latter case). In the case of the ColorMNIST dataset, we consider two classification tasks: digit classification (10 classes) and color classification (7 classes). We construct the attack to fool the classifier. See Appendix C.2 for the complete list of the hyperparameters used.

In Tables 2, 3, we compare the proposed defence strategy with other methods in the literature. For MNIST and Fashion MNIST (Table 2), we observe that pure VAE with the proposed MCMC-based defence is more robust than  $\beta$ -TCVAE, while it does not influence the quality of the reconstructions

Table 3: Robustness results on Color MNIST dataset. We perform unsupervised attack with radius 0.1 (top) and 0.2 (bottom). We attack the encoder (left) and the downstream classification task (right). Higher values correspond to more robust models.

<sup>†</sup> Our implementation. <sup>\*</sup> Values reported in Cemgil et al. (2020), VAE implementation and evaluation protocol may differ.

$\ \varepsilon\ $	MSSSIM[ $\tilde{\mathbf{x}}^r, \tilde{\mathbf{x}}^a$ ] ↑		ADVERSARIAL ACCURACY ↑						MSE	FID		
			DIGIT		COLOR							
	0.1	0.2	0.0	0.1	0.2	0.0	0.1	0.2				
VAE	0.36 (0.03)	0.19 (0.02)	1.00 (0.00)	0.04 (0.03)	0.02 (0.02)	1.00 (0.00)	0.06 (0.03)	0.06 (0.03)	261	2.1		
VAE + HMC	0.96 (0.01)	0.90 (0.01)	1.00 (0.00)	0.16 (0.02)	0.11 (0.02)	1.00 (0.00)	0.68 (0.03)	0.62 (0.03)	261	2.1		
$\beta$ -TCVAE <sup>†</sup>	0.35 (0.02)	0.23 (0.02)	0.94 (0.04)	0.08 (0.04)	0.05 (0.03)	1.00 (0.00)	0.06 (0.03)	0.05 (0.02)	266	3.0		
SE <sub>0,1</sub> <sup>*</sup>	—	—	0.94 (N/A)	0.89 (N/A)	0.02 (N/A)	1.00 (N/A)	1.00 (N/A)	0.22 (N/A)	1372	13.0		
SE <sub>0,2</sub> <sup>*</sup>	—	—	0.95 (N/A)	0.92 (N/A)	0.87 (N/A)	1.00 (N/A)	1.00 (N/A)	1.00 (N/A)	1375	11.7		
AVAE <sup>*</sup>	—	—	0.97 (N/A)	0.88 (N/A)	0.55 (N/A)	1.00 (N/A)	1.00 (N/A)	0.88 (N/A)	1372	15.5		
SE <sub>0,1</sub> -AVAE <sup>*</sup>	—	—	0.97 (N/A)	0.94 (N/A)	0.25 (N/A)	1.00 (N/A)	1.00 (N/A)	0.60 (N/A)	1373	13.9		
SE <sub>0,2</sub> -AVAE <sup>*</sup>	—	—	0.98 (N/A)	0.94 (N/A)	0.80 (N/A)	1.00 (N/A)	1.00 (N/A)	0.83 (N/A)	1374	13.9		
AVAE-SS <sup>*</sup>	—	—	0.94 (N/A)	0.73 (N/A)	0.21 (N/A)	1.00 (N/A)	1.00 (N/A)	0.57 (N/A)	1379	12.4		

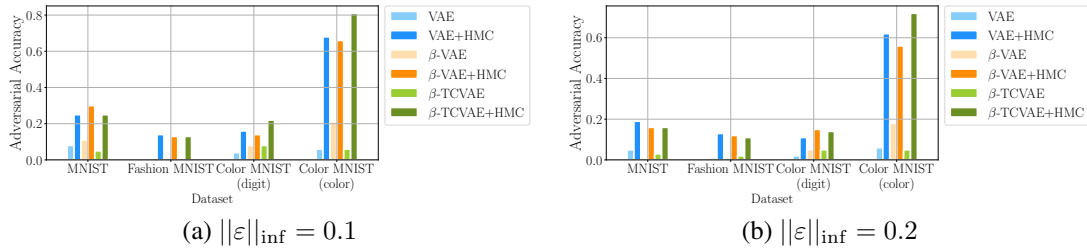


Figure 3: Improvement of the Adversarial Accuracy after proposed defence. We fix the attack radius to be equal to (a) 0.1 and (b) 0.2 (right column).

(see the MSE column). The latter model was shown to be more robust to the latent space attack (Willetts et al., 2021). Still, in our experiments (on different datasets), we could not observe the consistent improvement over pure VAE. It is worth mentioning that we have only implemented  $\beta$ -TCVAE with a single level of latent variables. For the ColorMNIST dataset (Table 3), we also compare the adversarial accuracy with the Smooth Encoders (SE) and Autoencoding Variational Autoencoder (AVAE) methods (Cemgil et al., 2019, 2020). We notice that these methods provide a higher adversarial accuracy. However, we have also observed a large discrepancy in terms of the MSE and FID scores of the model itself compared to our experiments, which we suspect is the result of a mistake in (Cemgil et al., 2019, 2020)<sup>2</sup> Lastly, we would like to highlight that our defence strategy can be also used with SE and AVAE methods without any restrictions.

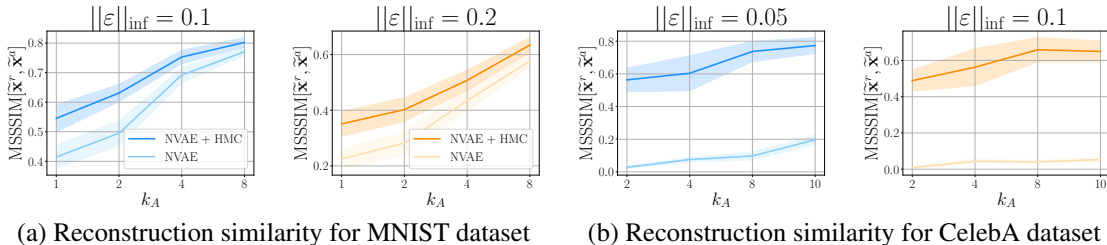


Figure 4: Robustness improvement for hierarchical model (NVAE) on (a) MNIST and (b) CelebA datasets for two different attack radiiuses.

## 4.2 Hierarchical VAE: NVAE

**Model and Datasets** In this section, we explore the robustness of the deep hierarchical VAE (NVAE) (Vahdat & Kautz, 2020), a recently proposed VAE with the state-of-the-art performance in terms of image generation. We attack models trained on MNIST and CelebA (Liu et al., 2015) datasets. We use the weights of the pre-trained NVAEs provided in the official NVAE implementation<sup>3</sup>.

<sup>2</sup>We have gotten in touch with the authors, who are kindly working with us to address this issue

<sup>3</sup>The code and model weights were taken from <https://github.com/NV1abs/NVAE>

**Attacks construction** Following (Kuzina et al., 2021) we construct adversarial attacks on hierarchical VAE by considering higher-level latent variables. That being said, we use latent variables  $\{z_{L-k_A}, z_{L-k_A+1}, \dots, z_L\}$  when constructing an attack (equation 4). Otherwise, we follow the same procedure we did for VAE with a single level of latent variables. We assume that the attacker has access to the model’s encoder and uses the symmetric KL-divergence as an objective. The radius of an attack is measured with the  $L_{\text{inf}}$  norm. For optimization, we use projected gradient descent with the number of iterations limited to 50 per point. Further details are reported in the Appendix C.2.

**Results** In Figure 4, we present reconstruction similarity of the reference and adversarial points for both datasets. We observe that the proposed defence consistently improves the robustness of the model to the adversarial attack. This result is in line with our theoretical considerations where a flexible class of variational posteriors could help to counteract adversarial attacks and, eventually, decrease the bias of the class of models measured in terms of the KL-divergence. Additionally, applying the MCMC can further help us to counteract the attack. In Figure 5 (the two bottom rows), we show how an adversarial point (c) is reconstructed without any defence (d) and with the proposed defence (e). In the depicted samples, we have used the top 10 latent variables ( $k_A = 10$ ) to construct the attack with a radius of 0.05.

## 5 Discussion

**Objective Function** For the unsupervised attack on the encoder, we use the symmetric KL-divergence to measure the dissimilarity. However, other options are possible, e.g., the forward or reverse KL-divergence or even  $L_2$  distance between the means. In our comparative experiments (see Appendix B.5), we observe that no single objective consistently performs better than others.

**What if attacker knows the defence strategy?** In Appendix B.3 we report results of the ablation study, where attacks on the encoder are constructed assuming that the attacker knows the defence strategy and attempts to use it during the attack construction. We observe that using MCMC during the attack construction does not help the attacker. On the contrary, it becomes harder to find a reasonable additive perturbation of the input.

**Attack radius** During the attack construction we seek to obtain a point that will have the most different latent representation or a different predicted class. However, it is also important that the point itself is as similar as possible to the initial reference point. In Appendix B.2, we visualize how the attacks of different radii influence the similarity between the adversarial and reference points. Based on these results, we have chosen the radii which do not allow adversarial points to deviate a lot from the reference (as measured by MSSSIM):  $\|\varepsilon\|_{\text{inf}} \leq 0.2$  for MNIST dataset (which goes in line with the previous works (Cemgil et al., 2019, 2020)) and  $\|\varepsilon\|_{\text{inf}} \leq 0.1$  for CelebA dataset.

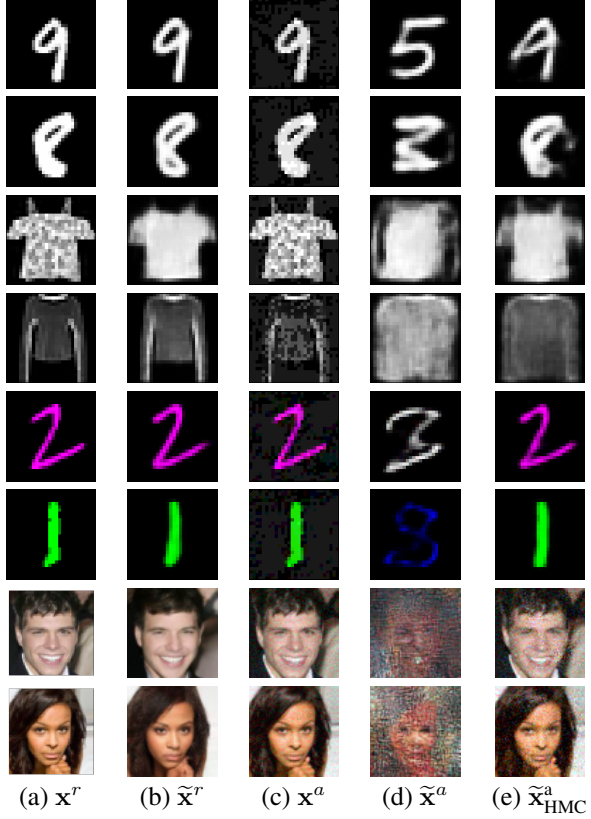


Figure 5: Example of the (a) Reference Point (b) Reconstruction of the reference point (c) Adversarial Point (d) Reconstruction of the Adversarial Point (e) Reconstruction of the Adversarial point after the proposed defence (HMC). All the adversarial examples are unsupervised attacks on the encoder.

**Number of steps during defence** For the defence, we have to select the number of MCMC steps that the defender performs. This parameter potentially can be critical. Following the theoretical analysis, the more steps in the MCMC procedure is taken, the tighter the bound is. On the other hand, typically we have time- and computational constraints to consider. In Appendix B.4, we show the method’s performance for the number of HMC steps ranging between 0 and 2000. There is a considerable jump in robustness between 0 and 100 steps. At the same time, we do not observe much improvement as we continue to increase the number of steps.

## 6 Conclusion and Future Work

In this work, we have explored the robustness of VAEs to adversarial attacks. We have suggested a theoretically justified method to defend a trained VAE against adversarial attacks. We experimentally validated our approach on a variety of datasets: both grey-scale (MNIST, Fashion MNIST) and colored (ColorMNIST, CelebA) data. We show that the defence improves the robustness of vanilla VAE models and its various modification:  $\beta$ -VAE,  $\beta$ -TCVAE and NVAE.

## Acknowledgements

Anna Kuzina is funded by the Hybrid Intelligence Center, a 10-year programme funded by the Dutch Ministry of Education, Culture and Science through the Netherlands Organisation for Scientific Research.

This work was carried out on the Dutch national e-infrastructure with the support of SURF Cooperative

## References

An, J. and Cho, S. Variational autoencoder based anomaly detection using reconstruction probability. *Special Lecture on IE*, 2(1):1–18, 2015.

Ballé, J., Minnen, D., Singh, S., Hwang, S. J., and Johnston, N. Variational image compression with a scale hyperprior. In *International Conference on Learning Representations*, 2018.

Barrett, B., Camuto, A., Willetts, M., and Rainforth, T. Certifiably robust variational autoencoders. *arXiv preprint arXiv:2102.07559*, 2021.

Bengio, Y., Courville, A., and Vincent, P. Representation learning: A review and new perspectives. *IEEE transactions on pattern analysis and machine intelligence*, 35(8):1798–1828, 2013.

Betancourt, M. A conceptual introduction to hamiltonian monte carlo. *arXiv preprint arXiv:1701.02434*, 2017.

Burda, Y., Grosse, R. B., and Salakhutdinov, R. Importance weighted autoencoders. In *International Conference on Learning Representations*, 2016.

Camuto, A., Willetts, M., Roberts, S., Holmes, C., and Rainforth, T. Towards a theoretical understanding of the robustness of variational autoencoders. In *International Conference on Artificial Intelligence and Statistics*, pp. 3565–3573. PMLR, 2021.

Cemgil, T., Ghaisas, S., Dvijotham, K. D., and Kohli, P. Adversarially robust representations with smooth encoders. In *International Conference on Learning Representations*. openreview.net, 2019.

Cemgil, T., Ghaisas, S., Dvijotham, K., Gowal, S., and Kohli, P. The autoencoding variational autoencoder. *Advances in Neural Information Processing Systems*, 33, 2020.

Chen, R. T., Li, X., Grosse, R., and Duvenaud, D. Isolating sources of disentanglement in variational autoencoders. *arXiv preprint arXiv:1802.04942*, 2018.

Child, R. Very deep VAEs generalize autoregressive models and can outperform them on images. In *International Conference on Learning Representations*, 2021.

Cremer, C., Li, X., and Duvenaud, D. Inference suboptimality in variational autoencoders. In *International Conference on Machine Learning*, pp. 1078–1086. PMLR, 2018.

Duane, S., Kennedy, A. D., Pendleton, B. J., and Roweth, D. Hybrid monte carlo. *Physics letters B*, 195(2):216–222, 1987.

Gondim-Ribeiro, G., Tabacof, P., and Valle, E. Adversarial attacks on variational autoencoders. June 2018.

Goodfellow, I. J., Shlens, J., and Szegedy, C. Explaining and harnessing adversarial examples. *arXiv preprint arXiv:1412.6572*, 2014.

Habibian, A., Rozendaal, T. v., Tomczak, J. M., and Cohen, T. S. Video compression with rate-distortion autoencoders. In *Proceedings of the IEEE/CVF International Conference on Computer Vision*, pp. 7033–7042, 2019.

Higgins, I., Matthey, L., Pal, A., Burgess, C., Glorot, X., Botvinick, M., Mohamed, S., and Lerchner, A. beta-vae: Learning basic visual concepts with a constrained variational framework. 2016.

Higgins, I., Pal, A., Rusu, A., Matthey, L., Burgess, C., Pritzel, A., Botvinick, M., Blundell, C., and Lerchner, A. Darla: Improving zero-shot transfer in reinforcement learning. In *International Conference on Machine Learning*, pp. 1480–1490. PMLR, 2017.

Jordan, M. I., Ghahramani, Z., Jaakkola, T. S., and Saul, L. K. An introduction to variational methods for graphical models. *Machine learning*, 37(2):183–233, 1999.

Kim, H. and Mnih, A. Disentangling by factorising. In *International Conference on Machine Learning*, pp. 2649–2658. PMLR, 2018.

Kingma, D. P. and Welling, M. Auto-encoding variational bayes. In *International Conference on Learning Representations, ICLR 2014*, 2014.

Kuzina, A., Welling, M., and Tomczak, J. M. Diagnosing vulnerability of variational auto-encoders to adversarial attacks. *ICLR, RobustML workshop*, 2021.

Liu, Z., Luo, P., Wang, X., and Tang, X. Deep learning face attributes in the wild. In *Proceedings of International Conference on Computer Vision (ICCV)*, December 2015.

Maaløe, L., Fraccaro, M., Liévin, V., and Winther, O. BIVA: A very deep hierarchy of latent variables for generative modeling. In *Advances in Neural Information Processing Systems*, February 2019.

Ranganath, R., Tran, D., and Blei, D. Hierarchical variational models. In *Proceedings of The 33rd International Conference on Machine Learning*, volume 48 of *Proceedings of Machine Learning Research*, pp. 324–333, New York, New York, USA, 2016. PMLR.

Rezende, D. J., Mohamed, S., and Wierstra, D. Stochastic backpropagation and approximate inference in deep generative models. In *International Conference on Machine Learning*, pp. 1278–1286. PMLR, 2014.

Sønderby, C. K., Raiko, T., Maaløe, L., Sønderby, S. R. K., and Winther, O. Ladder variational autoencoders. In *Advances in Neural Information Processing Systems*, volume 29, pp. 3738–3746. Curran Associates, Inc., 2016.

Vahdat, A. and Kautz, J. NVAE: A deep hierarchical variational autoencoder. In *Neural Information Processing Systems (NeurIPS)*, 2020.

Wang, Z., Simoncelli, E. P., and Bovik, A. C. Multiscale structural similarity for image quality assessment. In *The Thirty-Seventh Asilomar Conference on Signals, Systems & Computers, 2003*, volume 2, pp. 1398–1402. Ieee, 2003.

Willetts, M., Camuto, A., Rainforth, T., Roberts, S., and Holmes, C. Improving VAEs’ robustness to adversarial attack. In *International Conference on Learning Representations*, 2021.

Xiao, H., Rasul, K., and Vollgraf, R. Fashion-mnist: a novel image dataset for benchmarking machine learning algorithms. *arXiv preprint arXiv:1708.07747*, 2017.

## A Theory

We consider an attack, which has an additive structure:

$$\mathbf{x}^a = \mathbf{x}^r + \varepsilon, \quad (13)$$

$$\text{such that } \|\varepsilon\| \leq \delta, \quad (14)$$

where  $\delta$  is a radius of the attack.

In the vanilla VAE setup we will get the latent code by sampling from  $q_\phi(\mathbf{z}|\mathbf{x})$ . With our approach, instead, we get a sample from the following distribution:

$$q^{(t)}(\mathbf{z}|\mathbf{x}) = \int Q^{(t)}(\mathbf{z}|\mathbf{z}_0)q_\phi(\mathbf{z}_0|\mathbf{x})d\mathbf{z}_0, \quad (15)$$

where  $Q^{(t)}(\mathbf{z}|\mathbf{z}_0)$  is a transition kernel of MCMC with the target distribution  $\pi(\mathbf{z}) = p_\theta(\mathbf{z}|\mathbf{x}) \propto p_\theta(\mathbf{x}|\mathbf{z})p(\mathbf{z})$ .

**Lemma 1** Consider true posterior distributions of the latent code  $\mathbf{z}$  for a data point  $\mathbf{x}$  and its corrupted version  $\mathbf{x}^a$ . Then the KL-divergence between these two posteriors could be expressed using the small  $o$  notation of the radius of the attack, namely:

$$\text{KL}[p_\theta(\mathbf{z}|\mathbf{x}^r) \| p_\theta(\mathbf{z}|\mathbf{x}^a)] = o(\|\varepsilon\|). \quad (16)$$

*Proof*

Let us express the KL-divergence first with Bayes rule for the posteriors:

$$\text{KL}[p_\theta(\mathbf{z}|\mathbf{x}^r) \| p_\theta(\mathbf{z}|\mathbf{x}^a)] = \int p_\theta(\mathbf{z}|\mathbf{x}^r) \ln \frac{p_\theta(\mathbf{x}^r|\mathbf{z})p(\mathbf{z})p_\theta(\mathbf{x}^a)}{p_\theta(\mathbf{x}^a|\mathbf{z})p(\mathbf{z})p_\theta(\mathbf{x}^r)} d\mathbf{z} \quad (17)$$

$$= \underbrace{\int p_\theta(\mathbf{z}|\mathbf{x}^r) \ln \frac{p_\theta(\mathbf{x}^r|\mathbf{z})}{p_\theta(\mathbf{x}^a|\mathbf{z})} d\mathbf{z}}_{(a)} + \underbrace{\ln \frac{p_\theta(\mathbf{x}^a)}{p_\theta(\mathbf{x}^r)}}_{(b)}. \quad (18)$$

1. Let us introduce  $\log p_\theta(\mathbf{x}|\mathbf{z}) = g(\mathbf{x}, \mathbf{z})$ . Applying the Taylor expansion to  $g(\mathbf{x}^a, \mathbf{z})$  in the point  $\mathbf{x}^r$  yields:

$$g(\mathbf{x}^a, \mathbf{z}) = g(\mathbf{x}^r + \varepsilon, \mathbf{z}) = g(\mathbf{x}^r, \mathbf{z}) + \varepsilon^T \nabla_{\mathbf{x}^r} g(\mathbf{x}^r, \mathbf{z}) + o(\|\varepsilon\|). \quad (19)$$

Then, the log-ratio of two distributions is the following:

$$\ln \frac{p_\theta(\mathbf{x}^r|\mathbf{z})}{p_\theta(\mathbf{x}^a|\mathbf{z})} = g(\mathbf{x}^r, \mathbf{z}) - g(\mathbf{x}^a, \mathbf{z}) \quad (20)$$

$$= -\varepsilon^T \nabla_{\mathbf{x}^r} g(\mathbf{x}^r, \mathbf{z}) + o(\|\varepsilon\|). \quad (21)$$

Notice that  $\varepsilon^T \nabla_{\mathbf{x}^r} g(\mathbf{x}^r, \mathbf{z})$  is the dot product between  $\varepsilon$  and  $\nabla_{\mathbf{x}^r} g(\mathbf{x}^r, \mathbf{z})$ , i.e.,  $\varepsilon^T \nabla_{\mathbf{x}^r} g(\mathbf{x}^r, \mathbf{z}) = \langle \varepsilon, \nabla_{\mathbf{x}^r} g(\mathbf{x}^r, \mathbf{z}) \rangle$ .

Now, we can re-write the (a) part of (18) as follows:

$$(a) = - \int p_\theta(\mathbf{z}|\mathbf{x}^r) \langle \varepsilon, \nabla_{\mathbf{x}^r} g(\mathbf{x}^r, \mathbf{z}) \rangle d\mathbf{z} + o(\|\varepsilon\|) \quad (22)$$

$$= - \langle \varepsilon, \int p_\theta(\mathbf{z}|\mathbf{x}^r) \nabla_{\mathbf{x}^r} g(\mathbf{x}^r, \mathbf{z}) d\mathbf{z} \rangle + o(\|\varepsilon\|) \quad (23)$$

$$= - \langle \varepsilon, \int \frac{p_\theta(\mathbf{x}^r|\mathbf{z})p(\mathbf{z})}{p_\theta(\mathbf{x}^r)} \nabla_{\mathbf{x}^r} \ln p_\theta(\mathbf{x}^r|\mathbf{z}) d\mathbf{z} \rangle + o(\|\varepsilon\|) \quad (24)$$

$$= - \langle \varepsilon, \int \frac{p_\theta(\mathbf{x}^r|\mathbf{z})p(\mathbf{z})}{p_\theta(\mathbf{x}^r)} \frac{\nabla_{\mathbf{x}^r} p_\theta(\mathbf{x}^r|\mathbf{z})}{p_\theta(\mathbf{x}^r|\mathbf{z})} d\mathbf{z} \rangle + o(\|\varepsilon\|) \quad (25)$$

$$= - \langle \varepsilon, \int \frac{p(\mathbf{z}) \nabla_{\mathbf{x}^r} p_\theta(\mathbf{x}^r|\mathbf{z})}{p_\theta(\mathbf{x}^r)} d\mathbf{z} \rangle + o(\|\varepsilon\|) \quad (26)$$

$$= - \frac{\langle \varepsilon, \mathbb{E}_{p(\mathbf{z})} \nabla_{\mathbf{x}^r} p_\theta(\mathbf{x}^r|\mathbf{z}) \rangle}{p_\theta(\mathbf{x}^r)} + o(\|\varepsilon\|), \quad (27)$$

where we utilized the log-derivative trick in (25).

2. We can now apply a similar approach to calculate (b) part of (18). Let us denote  $\log p_\theta(\mathbf{x})$  as  $h(\mathbf{x})$ . Then calculating the Taylor series of  $h(\mathbf{x}^a)$  yields:

$$h(\mathbf{x}^a) = h(\mathbf{x}^r + \varepsilon) \quad (28)$$

$$= h(\mathbf{x}^r) + \varepsilon^T \nabla_{\mathbf{x}^r} h(\mathbf{x}^r) + o(\|\varepsilon\|). \quad (29)$$

Now, we can calculate the (b) part of (18) that gives the following log-ratio:

$$(b) = \ln \frac{p_\theta(\mathbf{x}^a)}{p_\theta(\mathbf{x}^r)} \quad (30)$$

$$= h(\mathbf{x}^a) - h(\mathbf{x}^r) \quad (31)$$

$$= \varepsilon^T \nabla_{\mathbf{x}^r} h(\mathbf{x}^r) + o(\|\varepsilon\|) \quad (32)$$

$$= \langle \varepsilon, \nabla_{\mathbf{x}^r} \ln p_\theta(\mathbf{x}^r) \rangle + o(\|\varepsilon\|) \quad (33)$$

$$= \langle \varepsilon, \frac{\nabla_{\mathbf{x}^r} p_\theta(\mathbf{x}^r)}{p_\theta(\mathbf{x}^r)} \rangle + o(\|\varepsilon\|) \quad (34)$$

$$= \frac{\langle \varepsilon, \nabla_{\mathbf{x}^r} \int p(\mathbf{z}) p_\theta(\mathbf{x}^r | \mathbf{z}) d\mathbf{z} \rangle}{p_\theta(\mathbf{x}^r)} + o(\|\varepsilon\|) \quad (35)$$

$$= \frac{\langle \varepsilon, \int p(\mathbf{z}) \nabla_{\mathbf{x}^r} p_\theta(\mathbf{x}^r | \mathbf{z}) d\mathbf{z} \rangle}{p_\theta(\mathbf{x}^r)} + o(\|\varepsilon\|) \quad (36)$$

$$= \frac{\langle \varepsilon, \mathbb{E}_{p(\mathbf{z})} \nabla_{\mathbf{x}^r} p_\theta(\mathbf{x}^r | \mathbf{z}) \rangle}{p_\theta(\mathbf{x}^r)} + o(\|\varepsilon\|). \quad (37)$$

Combining (a) and (b) together gives the claim, that is:

$$\text{KL}[p_\theta(\mathbf{z} | \mathbf{x}^r) \| p_\theta(\mathbf{z} | \mathbf{x}^a)] = -\frac{\langle \varepsilon, \mathbb{E}_{p(\mathbf{z})} \nabla_{\mathbf{x}^r} p_\theta(\mathbf{x}^r | \mathbf{z}) \rangle}{p_\theta(\mathbf{x}^r)} + o(\|\varepsilon\|) + \frac{\langle \varepsilon, \mathbb{E}_{p(\mathbf{z})} \nabla_{\mathbf{x}^r} p_\theta(\mathbf{x}^r | \mathbf{z}) \rangle}{p_\theta(\mathbf{x}^r)} + o(\|\varepsilon\|) \quad (38)$$

$$= o(\|\varepsilon\|). \quad (39)$$

■

**Lemma 2** The Total Variation distance (TV) between the variational posterior with MCMC for a given corrupted point  $\mathbf{x}^a$ ,  $q^{(t)}(\mathbf{z} | \mathbf{x}^a)$ , and the variational posterior for a given data point  $\mathbf{x}^r$ ,  $q_\phi(\mathbf{z} | \mathbf{x}^r)$ , can be upper bounded by the sum of the following three components:

$$\text{TV} \left[ q^{(t)}(\mathbf{z} | \mathbf{x}^a), q_\phi(\mathbf{z} | \mathbf{x}^r) \right] \leq \text{TV} \left[ q^{(t)}(\mathbf{z} | \mathbf{x}^a), p_\theta(\mathbf{z} | \mathbf{x}^a) \right] \quad (40)$$

$$+ \sqrt{\frac{1}{2} \text{KL}[p_\theta(\mathbf{z} | \mathbf{x}^r) \| p_\theta(\mathbf{z} | \mathbf{x}^a)]} \quad (41)$$

$$+ \sqrt{\frac{1}{2} \text{KL}[q_\phi(\mathbf{z} | \mathbf{x}^r) \| p_\theta(\mathbf{z} | \mathbf{x}^r)]}. \quad (42)$$

*Proof*

Total variation is a proper distance, thus, the triangular inequality holds for it. For the proof, we apply the triangular inequality twice. First, we use the triangle inequality for  $\text{TV}[q^{(t)}(\mathbf{z} | \mathbf{x}^a), q_\phi(\mathbf{z} | \mathbf{x}^r)]$ , namely:

$$\text{TV} \left[ q^{(t)}(\mathbf{z} | \mathbf{x}^a), q_\phi(\mathbf{z} | \mathbf{x}^r) \right] \leq \text{TV} \left[ q^{(t)}(\mathbf{z} | \mathbf{x}^a), p_\theta(\mathbf{z} | \mathbf{x}^r) \right] + \text{TV} \left[ p_\theta(\mathbf{z} | \mathbf{x}^r), q_\phi(\mathbf{z} | \mathbf{x}^r) \right]. \quad (43)$$

Second, we utilize the triangle inequality for  $\text{TV}[q^{(t)}(\mathbf{z} | \mathbf{x}^a), p_\theta(\mathbf{z} | \mathbf{x}^r)]$ , that is:

$$\text{TV} \left[ q^{(t)}(\mathbf{z} | \mathbf{x}^a), p_\theta(\mathbf{z} | \mathbf{x}^r) \right] \leq \text{TV} \left[ q^{(t)}(\mathbf{z} | \mathbf{x}^a), p_\theta(\mathbf{z} | \mathbf{x}^a) \right] + \text{TV} \left[ p_\theta(\mathbf{z} | \mathbf{x}^a), p_\theta(\mathbf{z} | \mathbf{x}^r) \right]. \quad (44)$$

Combining the two gives us the following upper bound on the initial total variation:

$$\text{TV} \left[ q^{(t)}(\mathbf{z}|\mathbf{x}^a), q_\phi(\mathbf{z}|\mathbf{x}^r) \right] \leq \text{TV} \left[ q^{(t)}(\mathbf{z}|\mathbf{x}^a), p_\theta(\mathbf{z}|\mathbf{x}^a) \right] + \text{TV} [p_\theta(\mathbf{z}|\mathbf{x}^a), p_\theta(\mathbf{z}|\mathbf{x}^r)] + \text{TV} [p_\theta(\mathbf{z}|\mathbf{x}^r), q_\phi(\mathbf{z}|\mathbf{x}^r)] \quad (45)$$

Moreover, the Total Variation distance is a lower bound of the KL-divergence (by Pinsker inequality):

$$\text{TV} [p(\mathbf{x}), q(\mathbf{x})] \leq \sqrt{\frac{1}{2} \text{KL} [p(\mathbf{x}) \| q(\mathbf{x})]}. \quad (46)$$

Applying Pinsker inequality to the second and the third terms in the right-hand part of equation 45 yields:

$$\text{TV} \left[ q^{(t)}(\mathbf{z}|\mathbf{x}^a), q_\phi(\mathbf{z}|\mathbf{x}^r) \right] \leq \text{TV} \left[ q^{(t)}(\mathbf{z}|\mathbf{x}^a), p_\theta(\mathbf{z}|\mathbf{x}^a) \right] + \sqrt{\frac{1}{2} \text{KL} [p_\theta(\mathbf{z}|\mathbf{x}^r) \| p_\theta(\mathbf{z}|\mathbf{x}^a)]} + \sqrt{\frac{1}{2} \text{KL} [q_\phi(\mathbf{z}|\mathbf{x}^r) \| p_\theta(\mathbf{z}|\mathbf{x}^r)]}. \quad (47)$$

■

**Theorem 1** The upper bound on the total variation distance between samples from MCMC for a given corrupted point  $\mathbf{x}^a$ ,  $q^{(t)}(\mathbf{z}|\mathbf{x}^a)$ , and the variational posterior for the given real point  $\mathbf{x}$ ,  $q_\phi(\mathbf{z}|\mathbf{x})$ , is the following:

$$\text{TV} \left[ q^{(t)}(\mathbf{z}|\mathbf{x}^a), q_\phi(\mathbf{z}|\mathbf{x}^r) \right] \leq \text{TV} \left[ q^{(t)}(\mathbf{z}|\mathbf{x}^a), p_\theta(\mathbf{z}|\mathbf{x}^a) \right] + \sqrt{\frac{1}{2} \text{KL} [q_\phi(\mathbf{z}|\mathbf{x}^r) \| p_\theta(\mathbf{z}|\mathbf{x}^r)]} + o(\sqrt{\|\varepsilon\|}). \quad (48)$$

*Proof*

Combining **Lemma 1** and **2** we get:

$$\underbrace{\text{TV} \left[ q^{(t)}(\mathbf{z}|\mathbf{x}^a), q_\phi(\mathbf{z}|\mathbf{x}^r) \right]}_{\text{Lemma 2}} \leq \text{TV} \left[ q^{(t)}(\mathbf{z}|\mathbf{x}^a), p_\theta(\mathbf{z}|\mathbf{x}^a) \right] + \sqrt{\frac{1}{2} \text{KL} [p_\theta(\mathbf{z}|\mathbf{x}^r) \| p_\theta(\mathbf{z}|\mathbf{x}^a)]} + \sqrt{\frac{1}{2} \text{KL} [q_\phi(\mathbf{z}|\mathbf{x}^r) \| p_\theta(\mathbf{z}|\mathbf{x}^r)]} \quad (49)$$

$$\underbrace{=}_{\text{Lemma 1}} \text{TV} \left[ q^{(t)}(\mathbf{z}|\mathbf{x}^a), p_\theta(\mathbf{z}|\mathbf{x}^a) \right] + \sqrt{\frac{1}{2} o(\|\varepsilon\|)} + \sqrt{\frac{1}{2} \text{KL} [q_\phi(\mathbf{z}|\mathbf{x}^r) \| p_\theta(\mathbf{z}|\mathbf{x}^r)]}. \quad (50)$$

Note that  $\sqrt{\frac{1}{2} o(\|\varepsilon\|)} = o(\sqrt{\|\varepsilon\|})$  that gives us the final expression:

$$\text{TV} \left[ q^{(t)}(\mathbf{z}|\mathbf{x}^a), q_\phi(\mathbf{z}|\mathbf{x}^r) \right] \leq \text{TV} \left[ q^{(t)}(\mathbf{z}|\mathbf{x}^a), p_\theta(\mathbf{z}|\mathbf{x}^a) \right] + \sqrt{\frac{1}{2} \text{KL} [q_\phi(\mathbf{z}|\mathbf{x}^r) \| p_\theta(\mathbf{z}|\mathbf{x}^r)]} + o(\sqrt{\|\varepsilon\|}). \quad (51)$$

■

## B Additional results

### B.1 Detailed results for $\beta$ -VAE and $\beta$ -TCVAE

In this section, we report the values that were used to produce Figures 2 and 3. We report mean values of the metric along with the corresponding standard deviations.

Table 4: Robustness results on MNIST, Fashion MNIST and Color MNIST datasets. We perform unsupervised attack with radius 0.1 (top) and 0.2 (bottom). We attack the encoder (left) and the downstream classification task (right). Higher values correspond to more robust models.

		MSSSIM[ $\tilde{\mathbf{x}}^r, \tilde{\mathbf{x}}^a$ ] $\uparrow$			ADVERSARIAL ACCURACY $\uparrow$				
		MNIST	FASHION MNIST	COLOR MNIST	MNIST		FASHION MNIST		
					MNIST	FASHION MNIST	COLOR	MNIST	
$\ \varepsilon\ _{\text{inf}}$	0.1	VAE	0.70 (0.02)	0.59 (0.03)	0.36 (0.03)	0.08 (0.04)	0.00 (0.01)	0.04 (0.03)	0.06 (0.03)
		+ HMC	<b>0.88 (0.01)</b>	<b>0.66 (0.03)</b>	<b>0.96 (0.01)</b>	0.25 (0.03)	<b>0.14 (0.02)</b>	0.16 (0.02)	0.68 (0.03)
		$\beta$ -VAE	0.75 (0.01)	0.52 (0.03)	0.50 (0.04)	0.11 (0.04)	0.00 (0.02)	0.08 (0.04)	0.21 (0.06)
	0.2	+ HMC	0.84 (0.01)	0.64 (0.03)	0.92 (0.03)	<b>0.30 (0.03)</b>	0.13 (0.02)	0.14 (0.02)	0.66 (0.04)
		$\beta$ -TCVAE	0.70 (0.02)	0.52 (0.03)	0.35 (0.02)	0.05 (0.03)	0.01 (0.01)	0.08 (0.04)	0.06 (0.03)
		+ HMC	0.79 (0.02)	<b>0.66 (0.03)</b>	<b>0.96 (0.01)</b>	0.25 (0.04)	0.13 (0.02)	<b>0.22 (0.03)</b>	<b>0.81 (0.02)</b>

## B.2 Which attack radius should be considered?

In our experiments, we use attacks with the radius 0.1 and 0.2 for all the models except for CelebA dataset, where radii 0.05 and 0.1 were considered. Here, we provide additional experiment to justify this choice. In Figure 6 (a) we show how the similarity between the reference point and the adversarial point. We observe that for CelebA the similarity drops faster than for the MNIST. Further, if we look at the example plotted in Figure 7, we can clearly notice that with the radius 0.2 CelebA image is already containing a lot of noise. At the same time, we observe (Figure 6 (b)) that reconstruction similarity, which indicates the success of the attack, drops relatively fast when the radius of the attack increases.

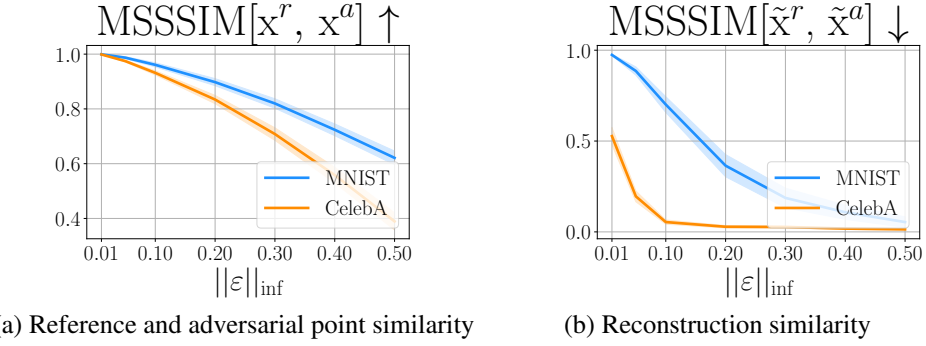


Figure 6: Average images similarity (a) before it is passed to VAE and (b) after image is encoded and decoded back. We consider unsupervised attack on the encoder with the radiuses ranging from 0.01 to 0.5 for MNIST and CelebA datasets.

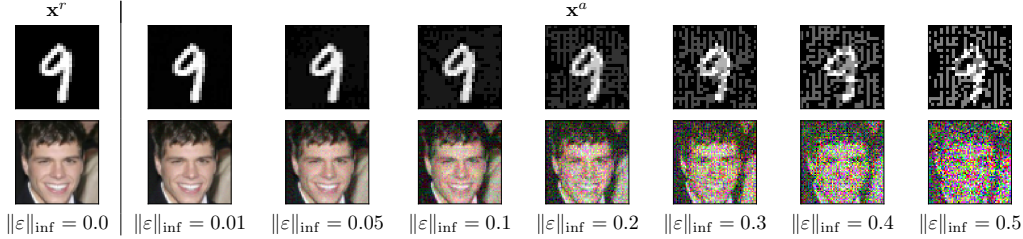


Figure 7

### B.3 What if the attacker knows the defence strategy?

In our experiments we relied on the assumption that attack does not take into account the defence strategy that we use. We believe that it is reasonable, since defence requires access to the decoder part of the model ( $p_\theta(x|z)$ ), which is not necessarily available to the attacker.

However, one may assume that the defence strategy is known to the attacker. In this case, it is reasonable to verify whether the robustness results change. In the conducted experiment we show that it is vastly more complicated to attack the encoder with taking the MCMC defence into account. We train the unsupervised attack (4). The attack has access to the encoder and MCMC defence:

$$f(x) = q^{(t)}(\mathbf{z}|\mathbf{x}) = \int Q^{(t)}(\mathbf{z}|\mathbf{z}_0)q_\phi(\mathbf{z}_0|\mathbf{x})d\mathbf{z}_0, \quad (52)$$

Then, given the attack radius  $\delta$ , we train the attack using the following objective:

$$\varepsilon^* = \arg \max_{\|\varepsilon\|_\infty < \delta} \|\tilde{z}^a - \tilde{z}^t\|^2, \quad (53)$$

$$\tilde{z}^a \sim q^{(t)}(\mathbf{z}|\mathbf{x}^r + \varepsilon), \quad (54)$$

$$\tilde{z}^t \sim q^{(t)}(\mathbf{z}|\mathbf{x}^r). \quad (55)$$

The similarity results of these attacks are plotted in Figure 9. We observe that the reconstructed reference and adversarial points have approximately the same similarity (as measured by MSSSIM) as the points themselves, which indicates that the attacks were unsuccessful.

However, if we use the same objective, but omit the MCMC step (e.g.  $t = 0$  in eq. 54 and 55), then, as observed in Figure 8, the attack becomes much more successful (Figure 8 (a)), but we can fix it with the proposed defence (Figure 8 (b)).

It is interesting to compare how the attacked points look in both cases, especially as we increase the radius of the attack. In Figure 10, we plot attack on two reference points for radius values in  $\{0.1, 0.6, 0.8, 1.0\}$ . When the attacker does not use MCMC (left), it just learns to add more and more noise to the image, which eventually makes it meaningless.

When we use MCMC during an attack, the situation is different. The adversarial input is almost indistinguishable from the reference point for a small radius. After each gradient update, the attacker runs a new MCMC, which moves point closer to the region of high posterior probability, but may follow a different trajectory every time. Eventually, it makes it harder to learn an additive perturbation  $\varepsilon$ . However, as we increase the attack radius, we observe a very interesting effect. Instead of meaningless noise, the attacker learns to change the digit. For instance, we see how 4 is transformed into 0 in the first example and into 9 in the second. This way, the attacker ensures that the MCMC will move the latent far away from the reference latent code, which now has a different posterior distribution.

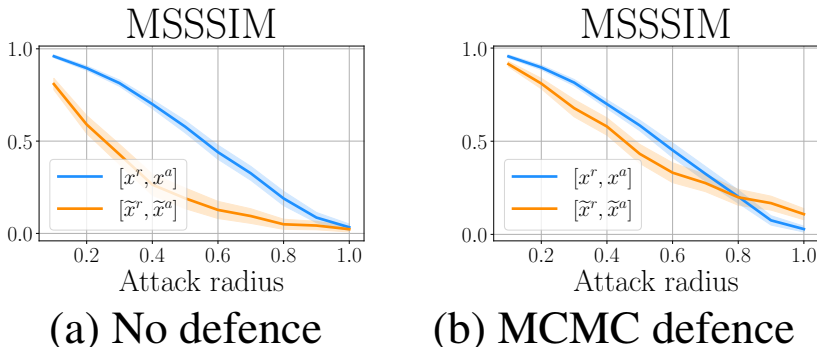


Figure 8: Adversarial attack, if attacker **does not use MCMC**. We report similarity of the reference and adversarial point before forward pass (blue) and after forward pass (orange).

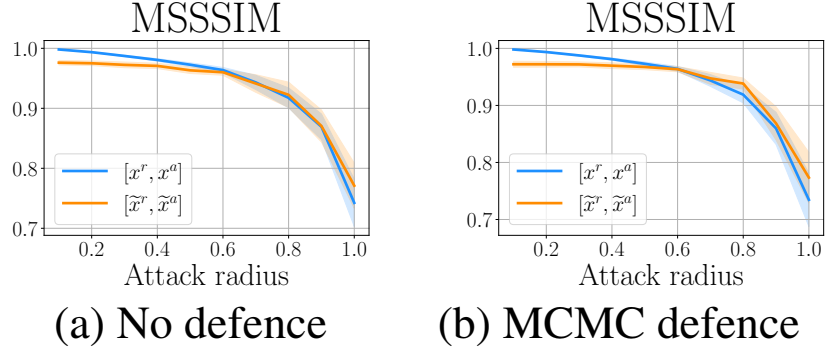


Figure 9: Adversarial attack, if attacker **uses** MCMC. We report similarity of the reference and adversarial point before forward pass (blue) and after forward pass (orange).

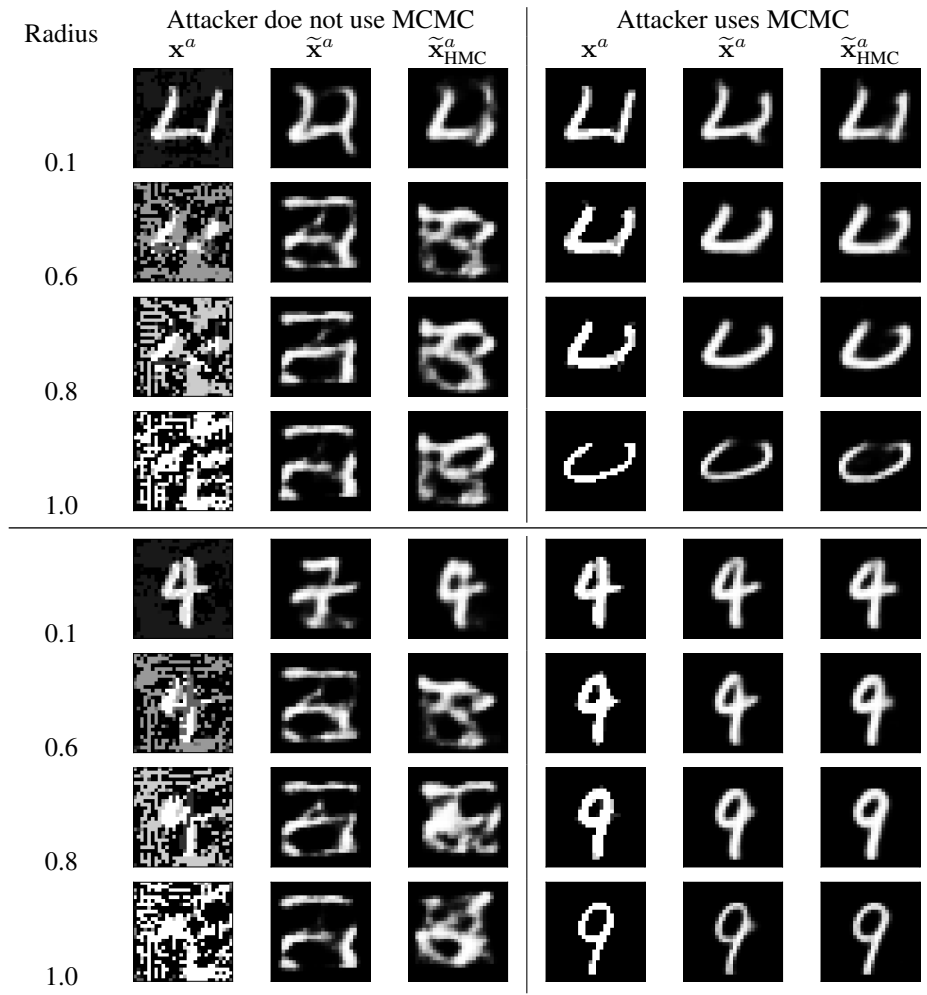
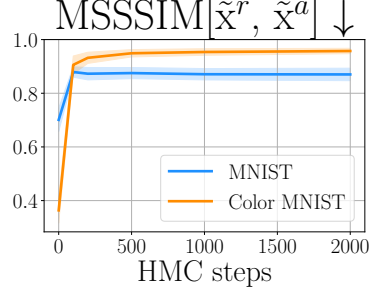


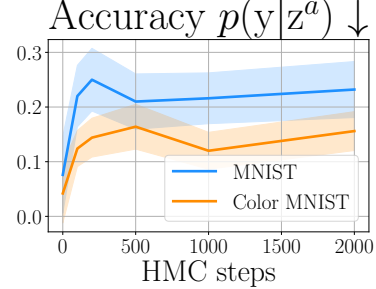
Figure 10: Examples of adversarial point and their reconstructions, when attacker does not use MCMC (left) and when attacker uses MCMC (right).

#### B.4 How many HMC steps are required for a defence?

One of the main hyperparameters of the proposed approach is number of steps of MCMC that the defender does. We have conducted experiments with MNIST and Color MNIST dataset to see how the robustness metrics change when we increase number of HMC steps from 0 to 200. As we can see from the Figure 11, there is always a considerable jump between 0 steps (no defence) and 100 steps (lowest number of steps considered). However, as we continue making steps, we do not observe further improvement of the metrics.



(a) Reconstruction similarity.

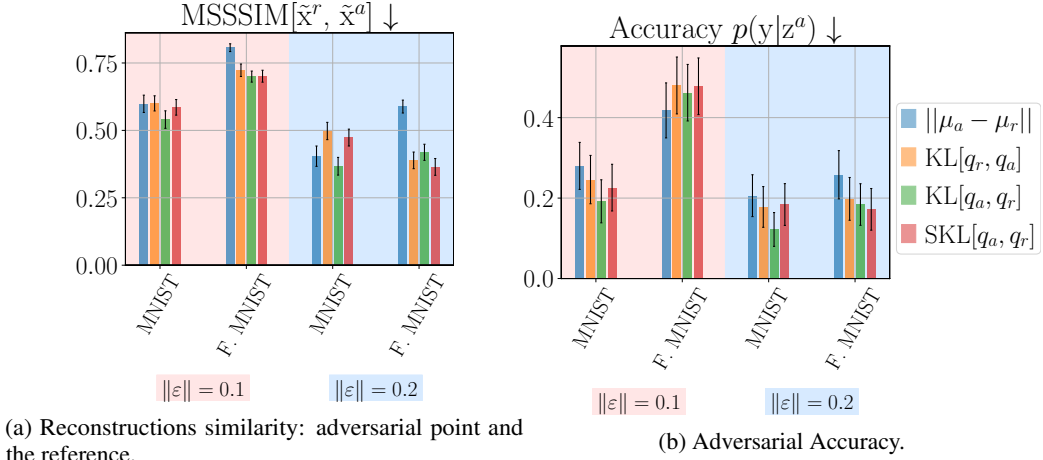


(b) Adversarial Accuracy (digit classification task).

Figure 11: Example of the reference point (leftmost column) and adversarial points for different raduises of the attack.

## B.5 Comparison of objective functions

This section compares different objective functions that can be used to construct adversarial attacks on VAE. In general, in both supervised and unsupervised setting, we need to measure the difference between variational posterior in the adversarial point  $q_a(z|x)$  and a point from the dataset (either a target or reference point). We consider a Gaussian encoder, and the simplest way to compare two Gaussian distributions is to measure the distance between their means. To take into account the variances, we can use the KL-divergence. It is a non-symmetric metric. Thus, we have two options: to use the forward or reverse KL. Finally, it is also possible to consider the symmetrical KL divergence that is an average between the two.



(a) Reconstructions similarity: adversarial point and the reference.

(b) Adversarial Accuracy.

Figure 12: Comparison of different objectives function used to train an attack. Arrows represent the direction of the successful attack.

In Figure 12, we measure how successful the attacks are in terms of the proposed metrics. We use arrows in the plot titles to indicate desirable values of the metric for a successful attack. We compare supervised and unsupervised attacks on VAE trained on MNIST and fashion MNIST datasets. We observe that there is no single objective function that consistently outperforms others.

## C Details of the experiments

### C.1 Training VAE models

**Architecture** We use the same fully convolutional architecture with latent dimension 64 for MNIST, FashionMNIST and ColorMNIST datasets. In Table 5, we provide detailed scheme of the architecture. We use  $\text{Conv}(3 \times 3, 1 \rightarrow 32)$  to denote convolution with kernel size  $3 \times 3$ , 1 input channel and 32 output channels. We denote stride of the convolution with  $s$ , padding with  $p$  and dilation with  $d$ . The same notation applied for the transposed convolutions ( $\text{ConvTranspose}$ ). ColorMNIST has 3 input channels, so the first convolutional layer in the encoder and the last of the decoder are slightly different. In this cases values for ColorMNIST are report in parenthesis with the red color.

Table 5: Convolutional architecture for VAE trained on MNIST, Fashion MNIST and ColorMNIST datasets.

Encoder	Decoder
$\text{Conv}(3 \times 3, 1 \rightarrow 32, s=2, p=1)$	$\text{ConvTranspose}(3 \times 3, 64 \rightarrow 128, s=1, p=0, d=2)$
$\text{ReLU}()$	$\text{ReLU}()$
$\text{Conv}(3 \times 3, 32 \rightarrow 64, s=2, p=1)$	$\text{ConvTranspose}(3 \times 3, 128 \rightarrow 96, s=1, p=0)$
$\text{ReLU}()$	$\text{ReLU}()$
$\text{Conv}(3 \times 3, 64 \rightarrow 96, s=2, p=1)$	$\text{ConvTranspose}(3 \times 3, 96 \rightarrow 64, s=1, p=1)$
$\text{ReLU}()$	$\text{ReLU}()$
$\text{Conv}(3 \times 3, 96 \rightarrow 128, s=2, p=1)$	$\text{ConvTranspose}(4 \times 4, 64 \rightarrow 32, s=2, p=1)$
$\text{ReLU}()$	$\text{ReLU}()$
$\mu_z \leftarrow \text{Conv}(3 \times 3, 128 \rightarrow 64, s=2, p=1)$	$\text{ConvTranspose}(4 \times 4, 31 \rightarrow 1 \rightarrow 1, s=2, p=1)$
$\log \sigma_z^2 \leftarrow \text{Conv}(3 \times 3, 128 \rightarrow 64, s=2, p=1)$	$\mu_x \leftarrow \text{Sigmoid}()$ ( <b>Identity()</b> )

**Optimization** We use Adam to perform the optimization. We start from the learning rate  $5e-4$  and reduce it by the factor of 2 if the validation loss does not decrease for 10 epochs. We train a model for 300 epochs with the batch size 128. In Table 6, we report the values of the test metrics for VAEs trained on MNIST, Fashion MNIST and Color MNIST.

For calculating the FID score, we use `torchmetrics` library: <https://torchmetrics.readthedocs.io/en/latest/references/modules.html#frechetinceptiondistance>.

Table 6: Test performance of the  $\beta$ -VAE and  $\beta$ -TCVAE with different values of  $\beta$ . Negative loglikelihood is estimated with importance sampling ( $k = 1000$ ) as suggested in (Burda et al., 2016).

$\beta$	MNIST		FASHION MNIST		COLOR MNIST		
	$-\log p(\mathbf{x})$	MSE	$-\log p(\mathbf{x})$	MSE	$-\log p(\mathbf{x})$	MSE	FID
1	<b>88.3</b>	578.6	<b>232.8</b>	814.3	<b>54.87</b>	261.3	2.09
$\beta$ -VAE	2	89.3	824.2	234.1	1021.1	55.6	365.6
	5	100.6	1485.1	241.8	1457.8	63.6	586.1
	10	126.8	2498.9	248.7	1842.3	88.7	936.2
$\beta$ -TCVAE	2	89.3	828.4	233.6	980.4	55.8	366.4
	5	96.7	1325.4	238.2	1024.6	63.0	574.8
	10	107.2	1686.1	247.5	1570.0	76.5	806.2

## C.2 Adversarial Attacks and Defence Hyperparameters

In Table 7, we report all the hyperparameter values that were used to attack and defend VAE models.

In all the experiments we randomly select reference points from the test dataset. We also ensure that the resulting samples are properly stratified — include an even number of points from each of the classes. For each reference point, we train 10 adversarial inputs with the same objective function but different initialization.

We use projected gradient descent to learn the adversarial attacks. Optimization parameters were the same for all the datasets and models. They are presented in Table 7.

We choose HMC to defend the model against the trained attack. We perform  $T$  steps of HMC with the step size  $\eta$  and  $L$  leapfrog steps. Where indicated, we adapt the step size after each step of HMC using the following formula:

$$\eta_t = \eta_{t-1} + 0.01 \cdot \frac{\alpha_{t-1} - 0.9}{0.9} \cdot \eta_{t-1}, \quad (56)$$

where  $\alpha_t$  is the acceptance rate at step  $t$ . This way we increase the step size if the acceptance rate is higher than 90% and decrease it otherwise. When adaptive steps size is used, a value in the table indicates the  $\eta_0$ .

Table 7: Full list of hyperparameters for attack construction and the defence.

	MNIST	VAE	Color MNIST	NVAE	
	MNIST	Fashion MNIST		MNIST	CelebA
Optimization (PGD)	# of reference points	50	50	50	20
	# of adversarial points	500	500	500	200
	Radius norm ( $\ \cdot\ _p$ )	inf	inf	inf	inf
	Radius	{0.1, 0.2}	{0.1, 0.2}	{0.1, 0.2}	{0.05, 0.1}
Defence (HMC)	Optimizer		SGD		
	Num. steps		50		
	$\varepsilon$ initialization		$\mathcal{N}(0, 0.2 \cdot I)$		
	Learning rate (lr)		1		
Defence (HMC)	Num. steps ( $T$ )	500	1000	1000	1000
	Step size $\eta$	0.1	0.05	0.05	1e-4
	Num. Leapfrog steps ( $L$ )	20	20	20	1
	Adaptive step size	True	True	True	False